2016

A unified view of tropical cyclogenesis and intensification

Kilroy, Gerard

Quarterly Journal of the Royal Meteorological Society Q. J. R. Meteorol. Soc. 143: 450–462, January 2017 A DOI:10.1002/qj.2934

RMetS
Royal Meteorological Society

A unified view of tropical cyclogenesis and intensification

Gerard Kilroy,[a]* Roger K. Smith[a] and Michael T. Montgomery[b]
[a]*Meteorological Institute, Ludwig Maximilians University of Munich, Germany*
[b]*Department of Meteorology, Naval Postgraduate School, Monterey, CA, USA*

*Correspondence to: G. Kilroy, Meteorological Institute, Ludwig-Maximilians University of Munich, Theresienstrasse 37, 80333 Munich, Germany. E-mail: gerard.kilroy@lmu.de

Idealized high-resolution numerical simulations of tropical cyclogenesis are presented in a model that represents deep convection by a warm rain process only. Starting with an initially weak, cloud-free, axisymmetric warm-cored vortex (maximum wind speed 5 m s^{-1} at a radius of 100 km), rapid vortex intensification begins after a gestation period on the order of 2 days. From a three-dimensional perspective, the genesis process is similar to that in the rotating convection paradigm for vortex intensification starting with a much stronger initial vortex (V_{max} = 15 m s^{-1}). The patterns of deep convection and convectively amplified cyclonic relative vorticity are far from axisymmetric during the genesis period. Moreover, the organization of the cyclonic relative vorticity into a monopole structure occurs at relatively low wind speeds, before the maximum local wind speed has increased appreciably. Barotropic processes are shown to play an important role in helping to consolidate a single-signed vorticity monopole within a few hours near the intensification begin time.

The rotating convection paradigm appears adequate to explain the basic genesis process within the weak initial vortex, providing strong support for a hypothesis of Montgomery and Smith that the genesis process is not fundamentally different from that of vortex intensification. In particular, genesis does not require a 'trigger' and does not depend on the prior existence of a mid-level vortex.

Key Words: tropical cyclone; hurricane; typhoon; spin-up; cyclogenesis; intensification

Received 7 June 2016; Revised 1 September 2016; Accepted 30 September 2016; Published online in Wiley Online Library 23 December 2016

1. Introduction

From a scientific viewpoint, the genesis (or birth) of a tropical cyclone is arguably one of the most fascinating problems in dynamical meteorology. At a fundamental level, one needs to explain the natural tendency for the emergence of a large-sale coherent convective-vortex structure from a much weaker initial disturbance. The precursor disturbances take the form of synoptic-scale tropical waves or other large-scale structures. Observations have long suggested that genesis is intrinsically a three-dimensional process involving the organization of deep convection. In the atmosphere, this organizational process competes with adverse factors that impede persistent deep convective activity and related vorticity organization. These adverse factors are primarily associated with the kinematic effect of vertical/horizontal shear deformation on the precursor disturbance and the intrusion of dry air into it.

One of the challenges in studying tropical cyclogenesis is that formation generally occurs over the ocean where conventional *in situ* observational data are limited. Until a few years ago, there had been only one notable field campaign devoted to collecting observational data on storm formation. This experiment was called the TEXMEX (Tropical EXperiment in MEXico) experiment. The research flights in TEXMEX were typically at 700 mb and thus the dropsonde data obtained were unable to document the convective environment through the troposphere. A review of what was known up to about 2008, including the TEXMEX experiment, is provided by Tory and Frank (2010). The situation changed with the organization in 2008 and 2010 of two major field campaigns aimed at collecting observations during the formation phase.

The first campaign was the Tropical Cyclone Structure 2008 (TCS08) experiment conducted in Northwest Pacific region during August–September 2008. This experiment had several research objectives, but for the component of the experiment that focused on the process of tropical cyclone formation, priority was given to developing storms before their classification as a tropical depression (Elsberry and Harr, 2008). The observations of formation included one particularly well-observed case of the genesis and intensification of typhoon *Nuri* (2008). Several research studies have been completed examining this notable event (Montgomery *et al.*, 2010; Raymond and López Carillo, 2011; Raymond *et al.*, 2011; Montgomery and Smith, 2012; Park *et al.* 2013; Lussier *et al.*, 2014).

The second campaign consisted of a trio of field experiments conducted in the northern summer of 2010 by the National Science Foundation (NSF), the National Aeronautics and Space Administration (NASA), and the National Oceanic and

Atmospheric Administration (NOAA) to investigate tropical cyclogenesis in the Caribbean and West Atlantic and the subsequent intensification of storms in these regions. While two of the experiments, the Genesis and Rapid Intensification Processes (GRIP) project of NASA and the Intensity Forecasting Experiment (IFEX) of NOAA, included intensification in their portfolio of objectives, the Pre-Depression Investigation of Cloud Systems in the Tropics (PREDICT) experiment was designed exclusively to study genesis and was by far the most comprehensive observational programme to do this (Montgomery *et al.*, 2012). Priority was given to developing storms prior to their classification as tropical depressions as defined by forecasters,* even when mature storms were present nearby.

An important aim of the PREDICT experiment was to gather data on developing and non-developing tropical disturbances to test the recently proposed marsupial model of tropical cyclogenesis in association with tropical easterly waves (Dunkerton *et al.*, 2009). The overarching hypothesis is that tropical depression formation is greatly favoured in the critical-layer (or 'pouch') region of the synoptic-scale, pre-depression wave or subtropical disturbance. Dunkerton *et al.* confirmed the main tenets of the marsupial model using global analyses, Tropical Rainfall Measuring Mission (TRMM) precipitation data and best-track data. However, details of how vortical convection is organizated was a facet of the theory that was not testable with these data. The gap in knowledge concerning the organization process was one of the main inspirations for the PREDICT experiment.

A summary of the scientific basis for the PREDICT experiment as well as some highlights of the data obtained are described by Montgomery *et al.* (2012). While the analysis of data obtained is still in progress, there have been already several studies examining the dynamical and thermodynamical structure of some of the genesis events documented (e.g. Davis and Ahijevych, 2012; Smith and Montgomery, 2012; Wang, 2012; Wang *et al.*, 2012; Fritz and Wang, 2013; Komaromi, 2013; Gjorgjievska and Raymond, 2014; Melhauser and Zhang, 2014). These studies provide a motivation for further modelling work.

In order to gain an understanding of the nature of vortical-convective organization, Hendricks *et al.* (2004) presented a numerical simulation and diagnoses of the genesis of hurricane *Diana* (1984) and found that a prominent feature of the genesis process was the development and aggregation of rotating deep convection. Subsequent modelling studies have confirmed that vortical convective clouds act as fundamental coherent structures during both the genesis and intensification process (Montgomery *et al.*, 2006, 2010; Nguyen *et al.*, 2008; Braun *et al.*, 2010; Fang and Zhang, 2010; Wang *et al.*, 2010; Davis, 2015). These locally buoyant clouds amplify the cyclonic vorticity of the precursor vortex by at least an order of magnitude (Saunders and Montgomery, 2004; Wissmeier and Smith, 2011; Kilroy and Smith, 2013). The vertical vorticity that is generated by the clouds outlives the convection that produced them in the first place.

In an aggregate sense, the buoyancy created by latent heating within these clouds drives a system-scale overturning circulation that contributes to the intensification of the system-scale vortex. The cyclonic vortical remnants tend to aggregate, in part due to quasi-barotropic dynamics and in part due to the diabatically driven overturning circulation. Some of these remnants will be intensified further by subsequent convective episodes. If the system-scale circulation strengthens, the vortical remnants will tend to be differentially sheared by the associated angular shear flow, and wrapped cyclonically around the precursor vortex. Stokes' theorem applied to a fixed area surrounding the convection implies that there will be an accompanying increase in strength of the system-scale circulation on account of the import of ambient absolute vorticity into it. When applied to a fixed area within the convective region, the import of vorticity into the area will lead also to an increase in the circulation. As the circulation progressively increases in strength, there is some elevation of the surface moisture fluxes. However, vortex intensification does not require the moisture fluxes to continually increase with surface wind speed (Montgomery *et al.*, 2009, 2015).

Motivated by the results of Montgomery *et al.* (2006), Nolan (2007) investigated the development of a tropical cyclone from a pre-existing, weak, warm-core vortex using high-resolution (2 km horizontal grid spacing) cloud-resolving simulations. He found that, when the relative humidity in the vortex core exceeds 80% over most of the depth of the troposphere, a mid-level vortex forms, contracts and intensifies. Once the mid-level vortex has reached a sufficient strength and the inner core is nearly saturated, a smaller-scale vortex forms very rapidly at the surface. This small vortex becomes the core of an intensifying tropical cyclone. Nolan proposed that 'the trigger for tropical cyclogenesis is the formation of this long-lasting updraught, which organises the low-level vorticity into a single coherent vortex through what might be considered either a repeated or continuous diabatic vortex merger process'. This conclusion would appear to support the widespread belief that tropical cyclogenesis is a finite-amplitude instability problem as articulated by Emanuel (1989). While, as discussed later, we do not exactly subscribe to this view of genesis, we would argue that the precursor wave pouch and its associated moist envelope is necessary and this is a finite-amplitude structure in which genesis takes place.

Much of the foregoing research forms what we believe is the basis for a unified view of tropical cyclogenesis and intensification (Montgomery and Smith, 2011). In this view, the separate stages proposed in previous significant studies and reviews (e.g. Frank, 1987; Emanuel, 1989; McBride, 1995; Karyampudi and Pierce, 2002; Tory and Frank, 2010) are unnecessary. The purpose of this article is to test this unified view of tropical cyclogenesis and intensification. The test will be conducted using a weak amplitude (maximum wind speed 5 m s^{-1} or less) cyclonic initial vortex embedded in a moist thermodynamic environment using either the Dunion moist tropical sounding (Dunion, 2011) or an averaged sounding taken from the PREDICT observations in the pre-*Karl* pouch region on 12 September, 2010. The time chosen for the pre-*Karl* sounding corresponds to approximately 2 days prior to the formation of tropical storm *Karl* (2010). The initial vortex used in these calculations, including the angular velocity and relative vertical vorticity of the initial vortex, are roughly comparable to those of the pre-*Karl* pouch circulation. This methodology ensures that the development occurs near the centre of the computational domain where there is a uniform grid mesh with the smallest grid spacing. This methodology ensures also that spin-up occurs in a reasonably short time providing for computational economy.

An outline of the remaining article is as follows. Section 2 discusses the details of the model configuration. Section 3 describes the simulations carried out. Section 4 presents analyses of the model results. Section 5 describes a series of sensitivity experiments. Section 6 provides a discussion of the results and their relation to prevailing ideas. Section 7 presents the conclusions.

2. The numerical model and experimental design

The simulations conducted and analyzed herein relate to the prototype problem for tropical cyclone intensification, which considers the evolution of a prescribed, initially cloud-free, axisymmetric vortex in a quiescent environment on an f-plane

*The glossary on the NOAA Hurricane Research Division website uses 'tropical cyclone' as 'the generic term for a non-frontal synoptic-scale low-pressure system over tropical or subtropical waters with organized convection (i.e. thunderstorm activity) and a definite cyclonic surface wind circulation'. Notably, this definition does not invoke any wind threshold. The same glossary defines a 'tropical depression' as 'a tropical cyclone with maximum sustained surface winds of less than 17 m s^{-1} (34 kt, 39 mph) and, in the Atlantic and Eastern Pacific Basins, a tropical storm as a tropical cyclone with surface winds between 17 and 33 m s^{-1}. Consistent with this definition, in this study we define genesis as the formation of a tropical depression with no formal threshold on wind speed.

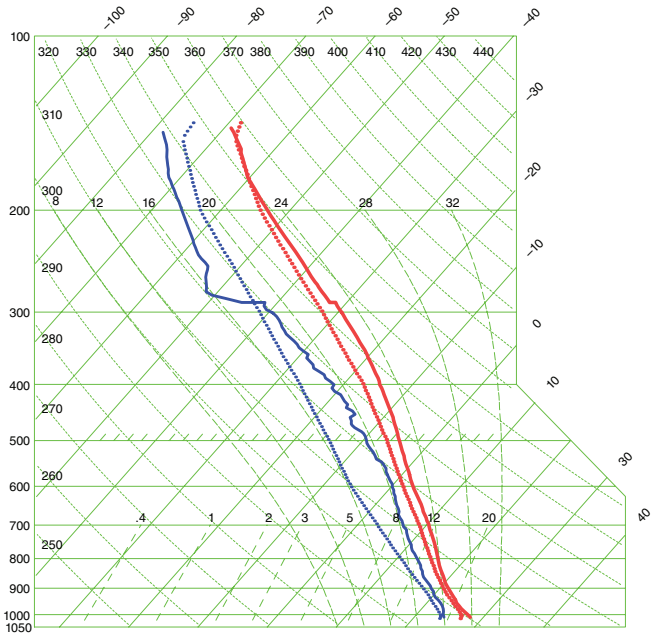

Figure 1. Skew $T-\log p$ diagram showing the temperature (right solid curve) and dew-point temperature (left solid curve) of the *Karl* pouch sounding used in this study. Also shown is the Dunion moist tropical sounding with temperature (right dotted curve) and dew-point temperature (left dotted curve), which is used for one of the sensitivity experiments.

as articulated in Nguyen *et al.* (2008). They are carried out using the numerical model CM1 version 16, a non-hydrostatic and fully compressible cloud model (Bryan and Fritsch, 2002)[†] in the three-dimensional configuration described by Persing *et al.* (2013), except that a larger inner grid-mesh region with constant grid spacing is used here. Specifically, the outer domain is 3000×3000 km in size with variable grid spacing reaching 10 km near the domain boundaries. The inner domain is 300×300 km in size and has a 500 m grid spacing. The domain has 40 vertical levels extending to a height of 25 km. The vertical grid spacing expands gradually from 50 m near the surface to 1200 m at the top of the domain.

Subgrid-scale parameters and exchange coefficients for momentum, moisture and heat are configured identically to those in Persing *et al.* (2013) based on the latest observational estimates of vertical and horizontal turbulent diffusivitities and air–sea exchange processes.

In brief, the model has prediction equations for the three components of the velocity vector, specific humidity, suspended liquid, perturbation Exner function, and perturbation density potential temperature, where perturbation quantities are defined relative to a prescribed hydrostatic basic state. A simple warm-rain scheme is used in which rain has a fixed fall speed of 7 m s^{-1}. For simplicity, ice microphysical processes and dissipative heating are omitted. The additional effects of including ice microphysics will be addressed in a forthcoming study.

Some of the model configuration was guided by data obtained in the pouch region of pre-genesis tropical storm *Karl* during the PREDICT field campaign. However, the aim of the article is to examine an idealized simulation and not to replicate the genesis of *Karl*.

The reference sounding is shown in Figure 1. It is a mean of 39 dropsonde soundings obtained on 12 September 2010 (Smith and Montgomery, 2012). This sounding has a Convective Available Potential Energy (CAPE)[‡] of 2028 J kg^{-1}, a Convection Inhibition (CIN)[§] of 47 J kg^{-1} and a Total Precipitable Water (TPW) value of 61 kg m^{-2}. The sea surface temperature (SST) is 29° C, typical of the Caribbean region at the time of *Karl*.

The calculations are carried out on an f-plane with the Coriolis parameter $f = 2.53 \times 10^{-5}$ s^{-1}, corresponding to 10° N. This value is lower than that of pre-*Karl* and was chosen because spin-up occurs sooner at low latitudes (Smith *et al.*, 2015), requiring less computational time.

Radiative effects are represented by adopting a simple Newtonian cooling approximation capped at 2 K per day, following Rotunno and Emanuel (1987). This approximation serves as a simple expedient for parametrizing the radiative-convective equilibrium process, which operates to maintain the ambient tropical sounding over realistic forecast time-scales of several days. In choosing this particular set-up, we purposely omit the more complex cloud-radiative feedback processes in the infrared wavelengths that have been suggested to accelerate the intensification process (e.g. Hakim, 2011; Nicholls and Montgomery, 2013) as well as the negative ocean feedback associated with storm-induced upwelling of colder ocean water below the storm which tends to retard the intensification process (e.g. Emanuel *et al.*, 2004).

To suppress the artificial reflection of internal gravity waves from the upper boundary, a Rayleigh damping layer is added at heights above 20 km. The e-folding time-scale for this damping is 5 min. Rayleigh damping is applied also within 100 km of the lateral boundaries, which are rigid walls.

In each experiment, the initial vortex is axisymmetric with a maximum tangential wind speed of 5 m s^{-1} (one sensitivity experiment has a maximum tangential wind speed of 3 m s^{-1}) at the surface at a radius of 100 km. A maximum wind speed of 5 m s^{-1} is comparable to the maximum tangential wind observed in the pre-*Karl* wave-pouch on 12 September, 1200 UTC (Davis and Ahijevych, 2012, their Figure 12b). The strength of the tangential wind decreases sinusoidally with height, vanishing at the top model level. The temperature field is initialized to be in gradient wind balance with the wind field using the method described by Smith (2006).

3. The simulations

We describe a total of five numerical experiments, the details of which are as follows. Expt 1, the control experiment, comprises the basis for the next section describing genesis and intensification. Expts 2 and 3 (referred to as 'P1' and 'P2', respectively) are identical to Expt 1 except there are random moisture perturbations of up to 0.5 g kg^{-1} applied from the surface to a height of 1 km. Expt 4 (referred to as the 'Dun' experiment) is the same as Expt 1, but a different environmental sounding is used, namely the Dunion moist tropical sounding (Figure 1, dotted curves). This sounding differs from the *Karl* pouch sounding in that it has a moderately drier mid-level environment (a TPW of 51.5 kg m^{-2} compared to 61 kg m^{-2} in the *Karl* sounding. Despite the drier environment, the Dunion sounding has a slightly larger CAPE averaged to 500 m (2104 J kg^{-1} compared to 2028 J kg^{-1}), although the minimum CIN is essentially the same. Expt 5, (referred to as the '3 m s^{-1}' experiment) is the same as the control vortex, except the initial vortex is weaker with a maximum tangential wind speed of 3 m s^{-1}. The results of Expts 2–5 and the motivation for these experiments are discussed in section 5.

[†]A complete description of the three-dimensional model and variable definitions is given by Bryan (2016), and of the axisymmetric version of CM1 by Bryan and Rotunno (2009).

[‡]CAPE is a parcel quantity that typically has a strong negative vertical gradient in the lower troposphere. For this reason, the values cited herein are based on an average for air parcels lifted from the surface and at 100 m intervals above the surface to a height of 500 m. Since the calculation of CAPE is a nonlinear function of temperature and moisture, we prefer this method to one based on averaged values of temperature and mixing ratio through a surface-based layer of air with some arbitrarily prescribed depth.

[§]Like CAPE, CIN is a quantity that refers also to an air parcel. Rather than computing an average up to 500 m as for CAPE, it seems physically more reasonable to examine the minimum value of CIN up to this level.

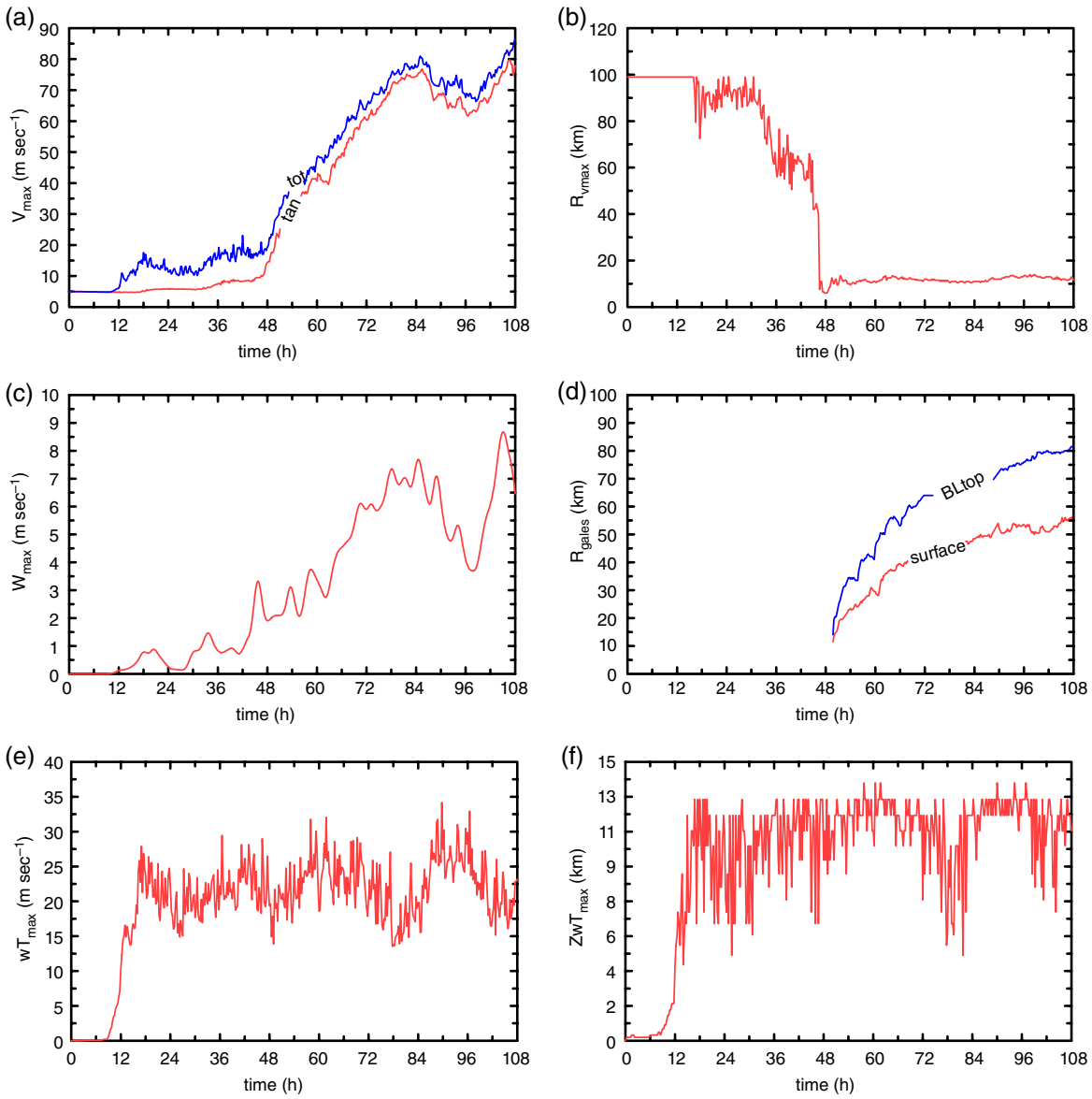

Figure 2. Time series for the control experiment of (a) maximum total wind speed (VT_{max}, blue curve labeled 'tot') and maximum azimuthally averaged tangential wind speed (V_{max}, red curve labeled 'tan'), (b) the radius R_{VMax} at which the maximum tangential wind speed occurs, and (c) the smoothed azimuthally averaged maximum vertical velocity. Panel (d) shows the outermost radius (R_{gales}) at which the azimuthally averaged tangential winds reach gale force (17 m s^{-1}) at a height of 1 km (blue curve labelled 'BLtop'), and the outermost radius at which the total wind at the surface reaches gale force (red curve labelled 'surface'). Panel (e) shows the maximum total vertical velocity (wT_{max}) anywhere in the domain, and (f) the height of this maximum.

4. Results: the control simulation

The main focus of the present article is the control simulation, the results of which are presented now. To set the scene we examine in section 4.1 time series of the maximum wind speed and various azimuthally averaged quantities characterizing the stages of vortex evolution. We follow in section 4.2 by showing the three-dimensional evolution of the vortex, focussing on horizontal depictions of the wind and vorticity structure, the vertical velocity at two levels and the surface pressure. We examine then in section 4.3 the importance of barotropic processes in the hours before intensification, before going on in section 4.4 to portray radius–height cross-sections of various azimuthally averaged fields. Finally we examine in section 4.5 the evolution of various system-averaged quantities. The vortex centre used for calculating the azimuthal average is determined by searching for the pressure minimum in a filtered pressure field, with a requirement that the vortex is not allowed to move more than 20 km in a single time step. This prevents the centre-finding algorithm from locking on to a localized region of strong convection. The centre location is taken to be independent of height.

4.1. *A summary of vortex evolution*

Figure 2 shows time series of the maximum total horizontal wind speed, VT_{max}, the maximum vertical velocity, wT_{max}, and of azimuthally averaged quantities including: the tangential wind speed, V_{max}; the radius R_{VMax} at which V_{max} occurs; the radius R_{gales} beyond R_{VMax} at which gale force winds (17 m s^{-1}) occur, both at the surface and at a height of 1 km[¶], and the smoothed maximum vertical velocity, w_{max}.

For the first 11 h, both VT_{max} and V_{max} show a slight decrease on account of friction, but with the onset of deep convection VT_{max} begins to increase with some small fluctuations.

As w_{max} increases in strength at around 30 h (Figure 2(c)), V_{max} begins to increase slowly also. An apparent turning point in the evolution occurs after about 45 h, when V_{max} begins to increase rapidly, followed a few hours later by a similar sharp increase in VT_{max}. We refer to this time as the 'intensification begin time', which coincides with a period of rapid intensification (RI). A major focus of section 4.2 is the change in vortex structure as this

[¶]The reasons for choosing both these altitudes are discussed in section 3.2 of Kilroy *et al.* (2016).

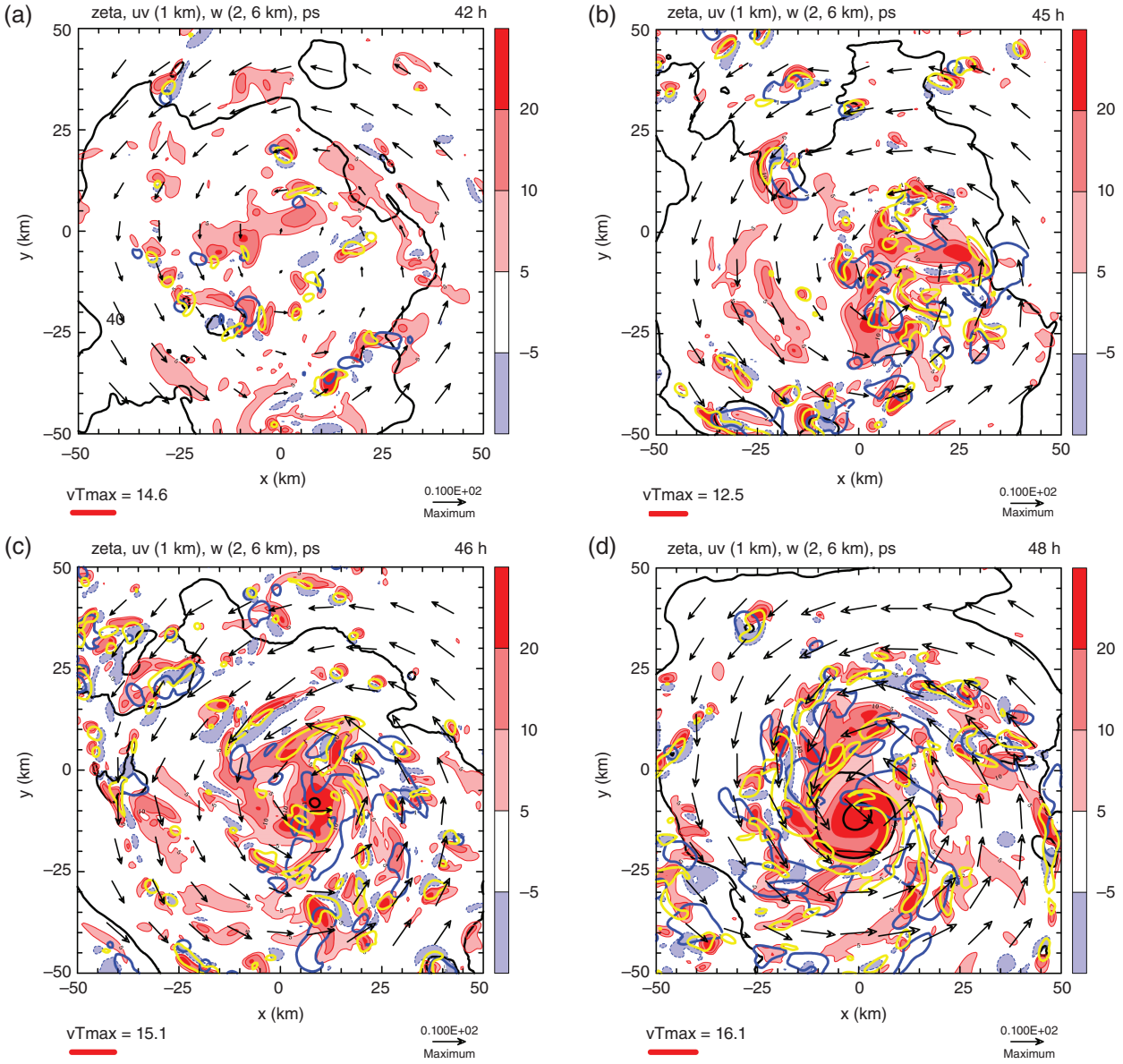

Figure 3. Horizontal cross-sections of relative vertical vorticity ($\times 10^{-4}$ s^{-1}, colour shading) and wind vectors at a height of 1 km for the control experiment, with 1 m s^{-1} contour of vertical velocity at heights of 2 km (blue) and 6 km (yellow). Also shown are surface pressure (black contours every 2 mb). The wind vectors are in relation to the maximum reference vector at the bottom right, while on the bottom left the maximum total wind speed in the domain plotted is given in m s^{-1}. The times shown are: (a) 42 h, (b) 45 h, (c) 46 h, (d) 48 h.

time is approached and passed. The onset of RI at about 45 h is accompanied by a sharp contraction of $R_{V\max}$ from about 60 km at 44 h to about 10 km at 48 h. During the subsequent intensification, $R_{V\max}$ increases slightly and then remains approximately within the range of 10–12 km. Typically, both $wT_{\max}$ and $w_{\max}$ occur at roughly the same height between 9 and 12 km during the mature phase.

Figure 2(d) shows that gale-force winds first develop at about 48 h and that R_{gales} progressively broadens with time. As expected, because of the frictional stress near the surface, the radius of gales is generally larger at a height of 1 km than at the surface. The calculations show that after approximately 60 h, R_{gales} is about 20–30 km larger at 1 km than its surface value.

4.2. *Evolution of vorticity*

Figure 3 shows horizontal cross-sections of vertical vorticity, wind vectors at a height of 1 km, and surface pressure at selected times straddling the intensification begin time. Contours of vertical velocity equal to 1 m s^{-1} at heights of 2 and 6 km are superimposed to indicate the location of strong updraughts at these levels. Panel (a) shows the fields at 42 h, 3 h before the intensification start time (about 45 h), while subsequent panels show the fields at (b) 45 h, (c) 46 h and finally (d) 48 h.

At 42 h, the centre of circulation as indicated by the velocity vectors lies near the centre of the computational grid, while the surface pressure field is quite diffuse at this time and the location of minimum pressure is not apparent at the 2 mb contour spacing shown. The value of $VT_{\max}$ is 14.6 m s^{-1} and occurs relatively far (at a radius of about 60 km) from the centre of circulation (recall that in the initial vortex, $R_{V\max}$ = 100 km). There are several irregularly shaped patches of locally enhanced vertical vorticity; the larger ones in area lie in a westsouthwest to eastnortheast oriented strip to the north of the vortex centre and in a sector to the southwest of the vortex centre. These are largely a result of the stretching of ambient vortex vorticity by previous and also current deep convective cells. There are a few patches of negative vertical vorticity also. These are associated with the tilting of horizontal vorticity into the vertical by convective updraughts and downdraughts (cf. Montgomery *et al.*, 2006; Kilroy and Smith, 2016), which tends to produce dipole structures. A few such dipoles are evident beneath strong updraughts at 2 km or 6 km height, for example near (18, −5 km), (0, 18 km) and (−27.5, 35 km).

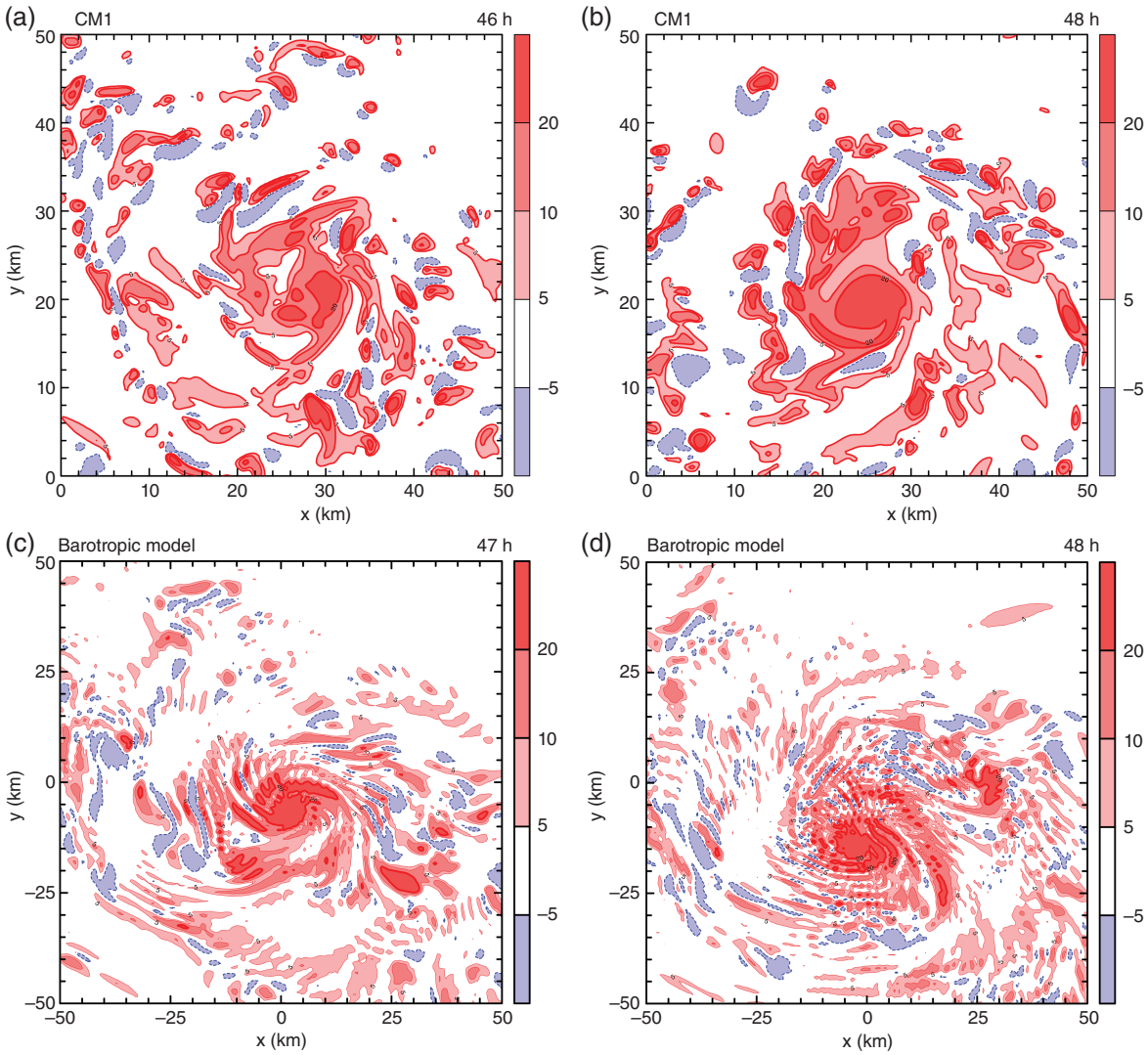

Figure 4. Horizontal cross-sections of relative vertical vorticity ($\times 10^{-4}$ s^{-1}, colour shading) in the CM1 output at (a) 46 h and (b) 48 h at 1 km altitude for the control experiment. Panels (c) and (d) show fields from the barotropic model at 47 and 48 h, respectively. The barotropic model is initialized with the vorticity and derived rotational winds from the CM1 model at 46 h and at a height of 1 km.

At 45 h (Figure 3(b)), the centre of circulation lies near (10, −10 km), while the surface pressure field is still diffuse and the location of minimum pressure is still not apparent. The value of VT_{max} is slightly less than at 3 h earlier: 12.5 m s^{-1}, although the winds have strengthened near the circulation centre, a reflection of the contraction of the vortex. Furthermore, the relative vorticity field has developed markedly. The patches of cyclonic vorticity have increased in size and consolidated around the vortex centre. Moreover, the area of patches with a magnitude exceeding $> 1 \times 10^{-3}$ s^{-1} has increased. There are many patches of negative vertical vorticity also, but these occur mostly on the periphery of the coherent region of cyclonic vorticity that surrounds the centre of circulation. The region with updraught speeds exceeding 1 m s^{-1} at 6 km height (the areas enclosed by yellow contours in the figure) has increased markedly also over the 3 h, indicating that deep convection has become more focussed.

By 46 h (Figure 3(c)), the cyclonic vorticity surrounding the centre of circulation has consolidated further and lies beneath an extensive updraught region at 6 km. $VT_{\max}$ at this time has increased by 2.6 m s^{-1} in 1 h, and a small closed contour of surface pressure has formed near the centre of circulation, indicating that the pressure has started to fall within the central core of high cyclonic vorticity.

Two hours later, at 48 h (Figure 3(d)), the monopole of high cyclonic vorticity near the centre of circulation has grown in size, $VT_{\max}$ at this time has increased by a further 1 m s^{-1} and the surface pressure has fallen further so that there are now two isobaric contours surrounding the centre of circulation. Similar plots at later times portray an acceleration of the intensification process with the appearance of more and more concentric surface isobars, an increase in $VT_{\max}$ (seen also in Figure 2(a)), and a further expansion of the core of enhanced cyclonic vorticity (not shown). The absence of (strong) anticylonic vorticity near the centre of the circulation corroborates the results of Kilroy and Smith (2016). This result negates the need to expel anticylonic vorticity from the core as argued by Nguyen *et al.* (2008).

The foregoing evolutionary features are similar to those that have been described earlier in studies of tropical cyclogenesis (Montgomery *et al.*, 2006) and in studies of vortex intensification starting from a much stronger initial vortex than the one here (e.g. Hendricks *et al.*, 2004; Nguyen *et al.*, 2008; Shin and Smith, 2008; Fang and Zhang, 2010; Persing *et al.*, 2013), leading to the important conclusion that *in a favorable pouch environment, there is no essential difference between the processes involved in tropical cyclone formation (or tropical cyclogenesis) and those involved in tropical cyclone intensification*. This finding supports the conjecture of Montgomery and Smith (2011). In particular, there is no obvious trigger for cyclogenesis (e.g. Nolan, 2007) and no finite amplitude threshold to be overcome (e.g. Emanuel, 1989).

Our results would appear to be more in line with the suggestion by Ooyama (1982, p. 371) that: 'It is unrealistic to assume that the formation of an incipient vortex is triggered by a special mechanism or mechanisms, or that genesis is a discontinuous change in the normal course of atmospheric processes. For the reason that is discussed below, it is far more natural to assume that

genesis is a series of events, arising by chance from quantitative fluctuations of the normal disturbances, with the probability of further evolution gradually increasing as it proceeds. According to this, view, the climatological and synoptic conditions do not directly determine the process of genesis, but may certainly affect the probability of its happening. With a better understanding of the mesoscale dynamics of organized convection, the range of statistical uncertainty can be narrowed down. Nevertheless, the probabilistic nature of tropical cyclogenesis is not simply due to lack of adequate data, but is rooted in the scale-dependent dynamics of the atmosphere'.

It may be significant that the organization of the relative vorticity into a monopole structure occurs at relatively low wind speeds and before the pressure has fallen substantially. For example, the initial pressure minimum is 1006.0 mb, that at 45 h is 1005.0 mb and that at 48 h 1001.8 mb. While the total wind maximum does not increase appreciably from 42 to 48 h (14.6 m s^{-1} compared to 16.1 m s^{-1}), there is a more substantial increase in the azimuthally averaged tangential wind maximum between these times (8.3 m s^{-1} compared to 14.4 m s^{-1}) and the structure of the wind field changes dramatically (compare Figures 3(a) and (d)).

4.3. *Barotropic processes*

In an effort to understand the evolution of the vorticity field, we examine first the role of barotropic processes. Figure 4 shows horizontal cross-sections of vertical vorticity from the barotropic model at (c) 47 h and (d) 48 h starting from the vorticity distribution in the CM1 output at (a) 46 h. For comparison, (b) shows the vorticity distribution in the CM1 output at 48 h. It is evident that the consolidation of vorticity around the nascent vorticity maximum is captured reasonably well by a barotropic process, although the central core of cyclonic vorticity is more extensive in the CM1 model, a reflection of the influx of vorticity and its amplification by stretching induced by deep convection.

It is found that the barotropic consolidation process does not occur within a 5 h period when starting from the vorticity distributions at earlier times (42, 43, 44, 45 h) when the patches of convectively amplified vorticity are more widely separated, or it occurs more slowly than starting at later times (not shown). This behaviour is reminiscent of the barotropic interaction of two patches of vorticity which, if close enough together, undergo irreversible merger, otherwise they simply rotate about each other (Melander *et al.*, 1987; Dritschel and Waugh, 1992). While the situation here with multiple vortices is more complicated, the barotropic calculations suggest a similar behaviour in which, at some point, the individual patches of convectively induced cyclonic vorticity merge together.

The merger of the individual patches of enhanced vorticity to form a monopole structure appears to mark a tipping point[‖] in the flow evolution. In the present CM1 calculations, this merger must be assisted by inflow associated with the convectively induced overturning circulation. The dominant importance of the overturning circulation in the intensification process is highlighted by the lack of intensification in any of the barotropic calculations as shown in Figure 5. This figure displays time series of the maximum azimuthally averaged tangential wind speed (V_{max}) in the barotropic model within a radius of 40 km for nine initial times at 1 h intervals beginning at 40 h and lasting for 4 h. Even around the intensification begin time, at 46 h and beyond there is no significant intensification of inner-core winds by barotropic processes alone. Thus, while barotropic processes play an important role in the merger of cyclonic vorticity anomalies to generate a monopole near the circulation centre, they appear to be unimportant in increasing the maximum wind speed. It follows that the inflow associated with the convectively induced

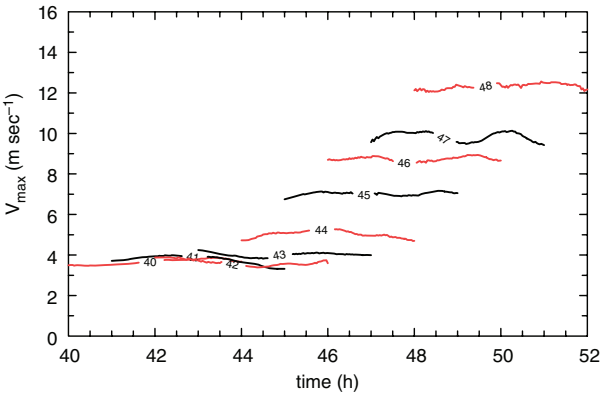

Figure 5. Time series of maximum azimuthally averaged tangential wind speed (V_{max}) in the barotropic model within a radius of 40 km from the vortex centre. The curves are labelled with the barotropic model start time, initiated with the vorticity fields from the control simulation at these times. We focus on V_{max} within a radius of 40 km to investigate any potential increases in V_{max} due to barotropic processes near the circulation centre.

overturning circulation in the CM1 simulation is the dominant mechanism for increasing V_{max}.

It is worth pointing out that, because of the stochastic nature of deep convection and the local amplification of vorticity by convection, there will a stochastic element to the vorticity aggregation process (section 5 discusses this matter further).

In section 4.4, we show evidence that the consolidation of the vorticity field as described above is accompanied by a local strengthening of the tangential circulation and a commensurate local increase in the boundary-layer inflow. We hypothesize that this inflow of moist air leads to local forced ascent, which reduces the convective inhibition, favouring the preferential development of deep convection in this location. In turn, deep convection leads to further amplification of the vortex.

4.4. *An azimuthally averaged view of vortex evolution*

Figure 6 shows vertical cross-sections of the azimuthally averaged, 3 h time-averaged tangential velocity at 12 h intervals to 72 h. The time averaging is centred on the time shown. While the time series in Figure 2(a) indicate little increase in V_{max} during the first 48 h, with most of that increase occurring after 45 h, the azimuthally averaged tangential wind fields in Figure 6 show considerable changes in structure during this time period. In particular, consistent with Figure 2(b), R_{Vmax} has already decreased from 100 km to about 20 km. Significantly, the formation of a mid-level vortex prior to genesis as found in some previous studies does not occur in this simulation.

During the next 12 h, from 48 to 60 h, there is a major change in vortex structure with a significant contraction of the tangential wind field and the appearance of the maximum wind at a radial distance of only 10 km from the axis at an altitude of barely 200 m (Figure 6(e)). By 72 h (Figure 6(f)), the vortex has intensified further, but with no additional contraction of the wind field. At this stage there is a second tangential wind maximum at an altitude of about 3 km.

Figure 7 shows vertical cross-sections of the azimuthally averaged, 3 h time-averaged radial velocity <u>, vertical velocity <w>, and absolute angular momentum M, at 12 h intervals from 36 to 72 h. The time averaging is centred on the time shown.

The radial and vertical velocity fields at 36 h highlight the system-scale overturning circulation generated by the collective effects of deep convection: there is inflow in the lower troposphere below about 7 km with the maximum inflow around 3 km in altitude and outflow in the upper troposphere with a maximum outflow at a height of about 12.5 km (Figure 7(a)). Broad-scale ascent with <w> > 0.1 m s^{-1} occurs through much of the domain shown, with maximum ascent at a radius of about 60 km and an altitude of about 10 km at this time (Figure 7(b)).

[‖]Dictionary.com defines a 'tipping point' as 'the culmination of the build-up of small changes that affects a big change'.

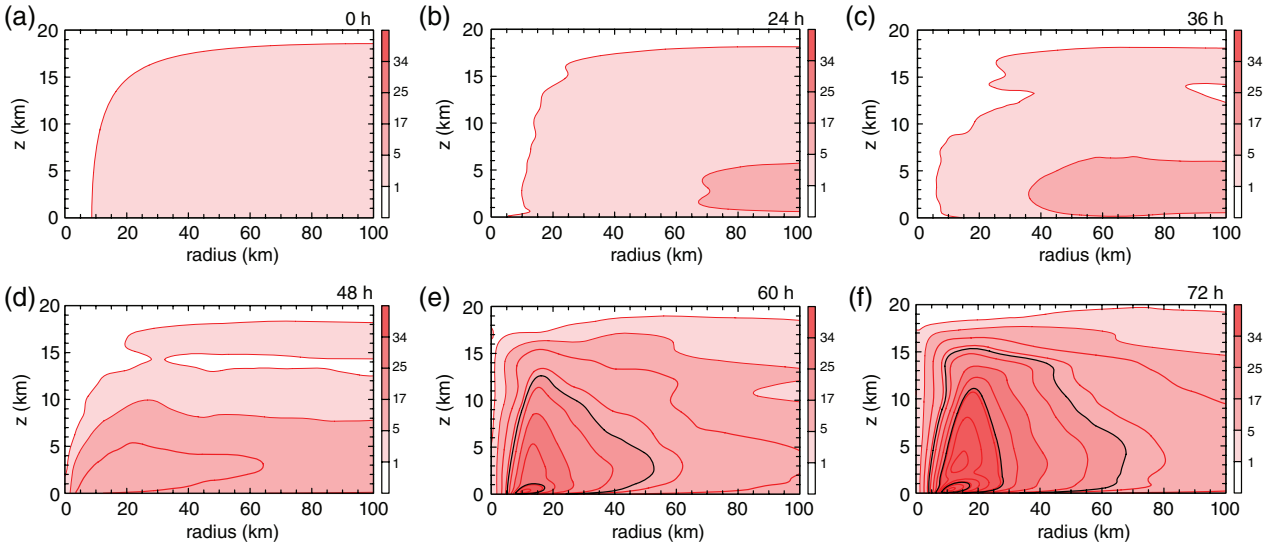

Figure 6. Vertical cross-sections of the azimuthally averaged, 3 h time averaged tangential velocity at (a) 0 h, (b) 24 h, (c) 36 h, (d) 48 h, (e) 60 h, and (f) 72 h in the control experiment. Red contours are at 5 m s^{-1} intervals. Additional black contours appear at 17, 34 and 51 m s^{-1}.

The angular momentum surfaces are bowed inwards in the lower troposphere where the inflow is a maximum, reflecting the approximate material conservation of M above the boundary layer (Figure 7(c)).

Just after the intensification begin time (48 h), the region with $<w>> 0.1$ m s^{-1} has migrated inwards, with the maximum of 1.3 m s^{-1} now closer to 25 km in radius (Figure 7(e)). This migration can be attributed to the organization of deep convection by the strengthening vortex circulation. Consistent with mass continuity, the inflow has strengthened at inner radii compared with 12 h previously and the outflow has strengthened in the upper troposphere (Figure 7(d)). In turn, the strengthening inflow has led to a further inward displacement of the M-surfaces in the lower troposphere (Figure 7(f)).

In section 4.2, we foreshadowed the linkage between the consolidation of the vorticity field with a local strengthening of the tangential circulation and a commensurate local increase in the boundary-layer inflow. Figure 7(g) reveals a strong radially localized inflow layer within about 50 km of the vortex axis with a small region of enhanced outflow just above extending to a radius of about 20 km. The beginning of this structure is seen at 48 h (Figure 7(d)). These features are evidence that the boundary layer is beginning to exert an important influence on flow at these radii, even around the intensification begin time. At 60 h, in the region of enhanced outflow, Figure 7(h) shows an enhanced upflow out of the boundary layer, which then extends into the upper troposphere. This upflow reflects the existence of deep convection in this radial band.

As in the tangential wind field, there are significant structural changes in the radial and vertical velocity fields following the onset of RI (compare Figures 7(g)–(i) with (d)–(f), respectively). Even at 60 h, the vertical velocity shows a radially narrow annular region of strong ascent ($<w> > 2$ m s^{-1}) reminiscent of an eyewall with a narrow region of marked subsidence along its inner edge (Figure 7(h)). The inflow has strengthened markedly in a shallow frictional boundary layer near the surface and there is outflow in the eyewall (Figure 7(g)), indicating an outward slope of the eyewall. There is strong outflow in a shallow layer just above where the boundary-layer inflow terminates, indicative of the fact that the flow ascending out of the boundary layer into the eyewall is supergradient (e.g. Smith *et al.*, 2009). Note that there is a low-level maximum in vertical velocity where the boundary-layer inflow terminates, an indication of strong vertical pressure gradients that would be required to accelerate the ascending flow in this region. Again, the M-surfaces have continued to move inwards in the lower troposphere and have become more erect in the eyewall (Figure 7(i)). Significantly, there is radial outflow across a broad radial band outside the main eyewall updraught as defined above. Thus the classical mechanism for spin-up whereby M surfaces are advected inwards in the lower troposphere above the frictional boundary layer does not operate to spin up the eyewall, nor does it act to spin up the maximum tangential wind speed, which occurs within the region of strong boundary-layer inflow (compare Figure 6(e) with Figure 7(g)).

By 72 h, the vortex has strengthened further and shows many features of a mature tropical cyclone. In particular, the boundary-layer inflow has strengthened, as has the patch of outflow above it where the inflow terminates and the air ascends into the eyewall. Now there is a prominent layer of enhanced inflow just above the patch of outflow. These inflow and outflow features, which extend up to about 4 km, are indicative of a standing inertial wave in the lower part of the eyewall as the eyewall updraught adjusts towards gradient wind balance (e.g. Smith *et al.*, 2009; Smith and Montgomery, 2010; Montgomery and Smith, 2017). The region of moderate ascent outside the main eyewall updraught ($<w>> 0.1$ m s^{-1}) has contracted radially inwards (Figure 7(k)) and strengthened, although the inflow has weakened through much of the troposphere below about 10 km, except in the frictional boundary layer. The weakening inflow above the boundary layer is presumably an indication that the increasing inertial instability accompanying the strengthening vortex is sufficient to weaken the convectively induced inflow. The strengthening boundary-layer inflow is consistent with a strengthening vortical flow above the boundary layer. With the continued inflow, above approximately 1.5 km height outside of the inner-core region, the M-surfaces have moved further inwards in the lower troposphere, which accounts for the expansion of the outer tangential circulation (Figure 6(f)).

4.5. *A system-averaged perspective of vortex evolution*

In order to gain a more complete picture of the genesis process, we consider now a system-averaged view. Figure 8 shows time–height cross-sections of system-averaged quantities within a column with horizontal cross-section 50 × 50 km^2, centred at the centre of the circulation. These include the deviations of temperature, water vapour mixing ratio and equivalent potential temperature from their respective values at the start of the time series, the relative humidity, the vertical mass flux, and the vertical component of relative vorticity. It is seen that, like the vorticity fields discussed in section 4.2, thermodynamic conditions in the column have evolved significantly before the RI stage. In particular, the

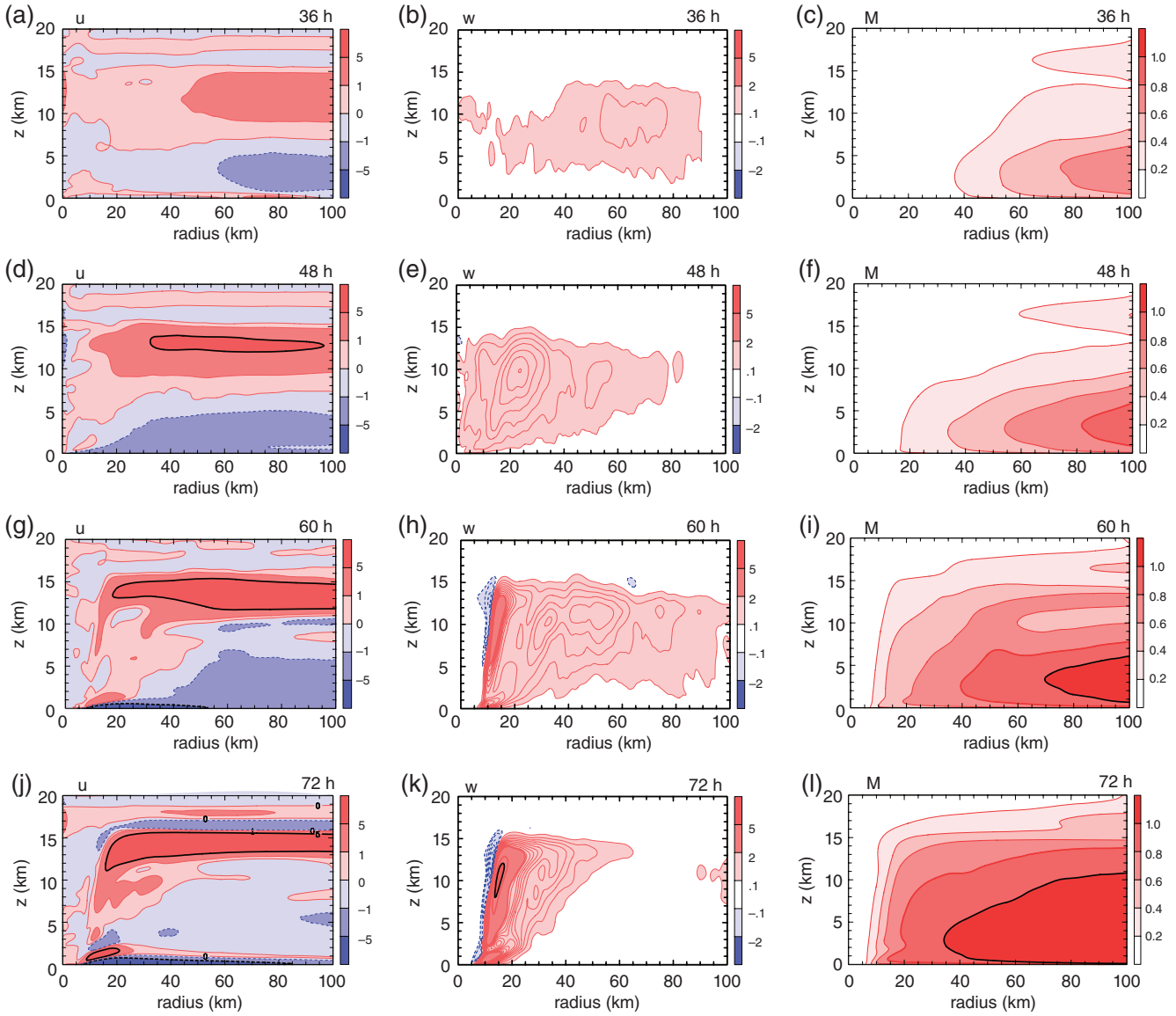

Figure 7. Vertical cross-sections of the azimuthally averaged, 3 h time averaged (a, d, g, j) radial velocity ($m\,s^{-1}$), (b, e, h, k) vertical velocity ($m\,s^{-1}$) and (c, f, i, l) absolute angular momentum at (a, b, c) 36 h, (d, e, f) 48 h, (g, h, i) 60 h, and (j, k, l) 72 h in the control experiment. Colour bars show the shading, and solid contours are positive, dashed contours negative. Contours for vertical velocity are at intervals of 0.2 $m\,s^{-1}$ from 0.1 to 2.0 $m\,s^{-1}$, then bolder contours every 2.0 $m\,s^{-1}$. Units for absolute angular momentum are 1×10^6 $m^2\,s^{-1}$. The thick black contour highlights regions of strong outflow (5 $m\,s^{-1}$) in (a, d, g, j), regions of strong upflow (5 $m\,s^{-1}$) in (b, e, h, k), and regions where absolute angular momentum is large (1×10^6 $m^2\,s^{-1}$) in (c, f, i, l).

mid-to-upper troposphere warms while the lower troposphere cools.

Generally, the troposphere moistens in an absolute sense, as evidenced by the increase of water vapour mixing ratio throughout the troposphere, but the relative humidity, after first increasing at most levels, begins to develop a mid-tropospheric minimum after about 56 h, presumably because, as the vortex becomes strong, it becomes also narrow so that the $50 \times 50\,km^2$ column begins to sample part of the subsiding branch of the overturning circulation, including the eye. Significantly, the mid-tropospheric θ_e and the tropospheric relative humidity both increase prior to RI. A similar result has been found in many earlier studies (e.g. Nolan, 2007 and references therein).

It is evident that the *preconditioning* of the $50 \times 50\,km^2$ column is accompanied by periods of positive vertical mass flux associated with deep convection. The convection leads at first to an amplification of the low-level vertical vorticity within the column, but the vorticity increases throughout the troposphere prior to the onset of RI. It may be worth pointing out that, since the calculations start with a relatively moist thermodynamic sounding, they may be expected to bypass a part of the 'preconditioning stage' that occurs in reality.

5. Sensitivity experiments

Figure 9(a) shows the evolution of V_{max} in Expts 2–5 detailed in section 3. The inclusion of moisture perturbations in P1 and P2 leads to small differences in the intensification begin time of at most a few hours compared with the control calculation. Such differences are to be expected following the studies of vortex intensification by Nguyen *et al.* (2008) and Shin and Smith (2008), and vortex genesis (Wang, 2014) and they may be attributed to the stochastic nature of deep convection in the model.

Of course, the differences between the evolution of V_{max} in the experiments with perturbed moisture may depend on both the magnitude and spatial scale of the initial moisture perturbations. This aspect has not yet been explored here because of the high computational cost. Using Dunion's mean tropical sounding ('Dun' experiment) delays the start time for intensification by about 8 h. When initiating with a weaker vortex, the start time for intensification is delayed further (Figure 9(b)). In the '3 $m\,s^{-1}$' experiment the intensification begin time is about 84 h, nearly 40 h longer than in the control and moisture perturbed experiments.

Figure 9(b) shows the evolution of the 2 h tendency, $dV_{max}(t) = V_{max}(t + 2\,h) - V_{max}(t)$ during the gestation and rapid intensification periods. In all experiments the intensification

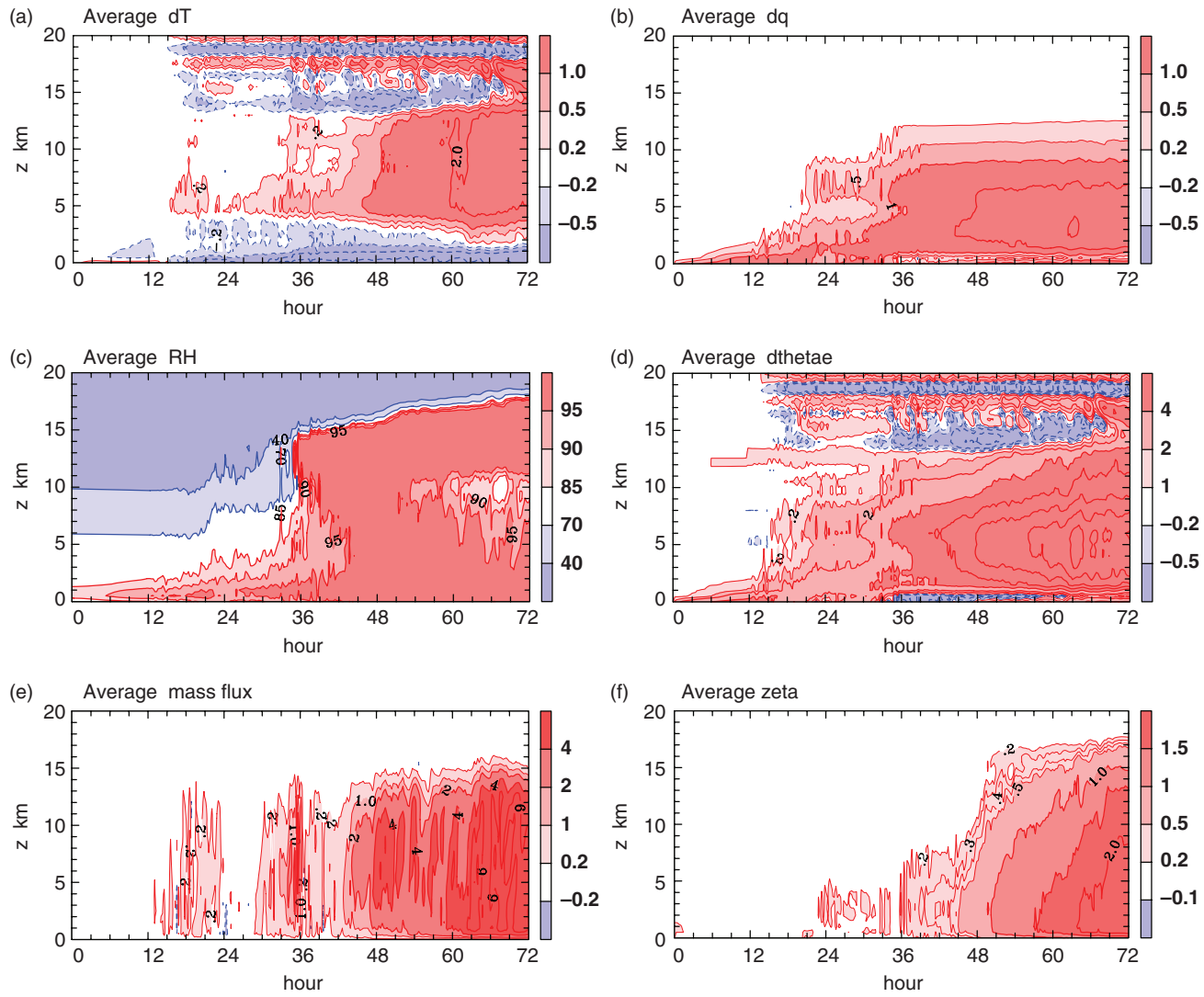

Figure 8. Time–height cross-sections of system-averaged quantities within a $50 \times 50\,\mathrm{km}^2$ column for the control experiment, centred on the domain centre: (a) the temperature deviation (K) from that at the start of the time series, (b) the water vapour mixing ratio difference ($\mathrm{g\,kg^{-1}}$) from that at the start of the time series, (c) the relative humidity (%), (d) the equivalent potential temperature deviation (K) from that at the start of the time series, (e) the vertical mass flux per unit area ($\mathrm{kg\,m^{-2}\,s^{-1}}$), and (f) the relative vorticity ($10^{-4}\,\mathrm{s^{-1}}$).

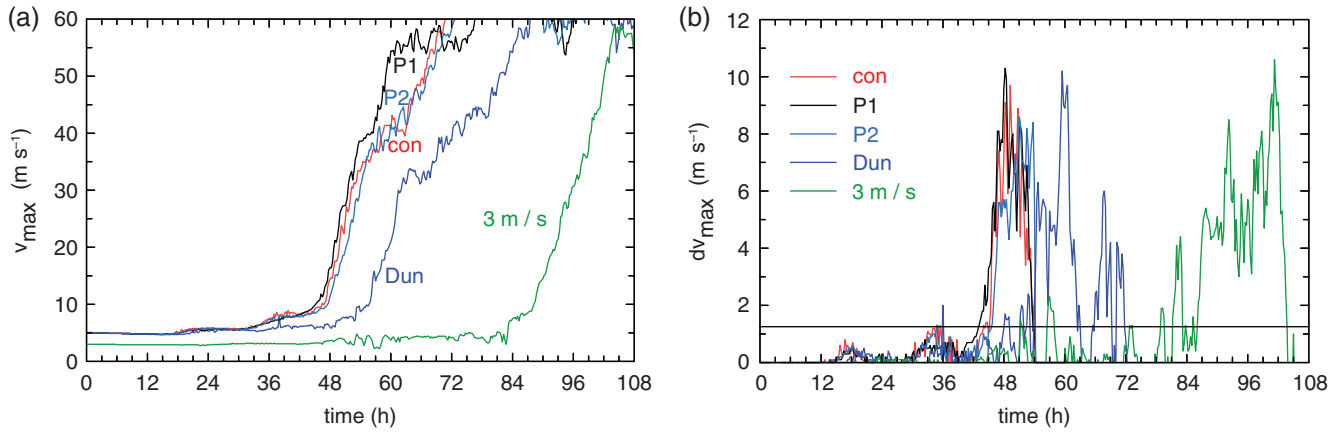

Figure 9. Time series from five experiments of (a) maximum azimuthally averaged tangential wind speed (V_{max}) and (b) the 2 h tendency, $dV_{max}(t) = V_{max}(t + 2\,\mathrm{h}) - V_{max}(t)$, during the gestation and rapid intensification periods. The horizontal line in (b) denotes an intensification rate of $15\,\mathrm{m\,s^{-1}}$ per day. The experiments are: the control (con; Expt 1), the two experiments similar to the control, but with perturbations to the initial boundary-layer moisture (P1 and P2; Expts 2 and 3), the one using the Dunion moist tropical sounding (Dun; Expt 4), and the one with a weaker initial vortex ($3\,\mathrm{m\,s^{-1}}$; Expt 5).

rate, when it begins, is rapid, with $dV_{max}(t)$ exceeding the forecaster's criterion** for RI rate ($15\,\mathrm{m\,s^{-1}}$ per day), at least when considering the maximum azimuthally averaged tangential wind component.

Despite the small magnitude in the moisture perturbations in P1 and P2, they have a significant impact on the detailed patterns of deep convection and the convectively induced patterns of vorticity. Figure 10 shows horizontal cross-sections of vertical vorticity, wind vectors at a height of 1 km and surface pressure

**Actually, the forecaster's criterion applies to the total 1 min (or 10 min) average total wind speed at a height of 10 m and requires the rate to persist for 1 day.

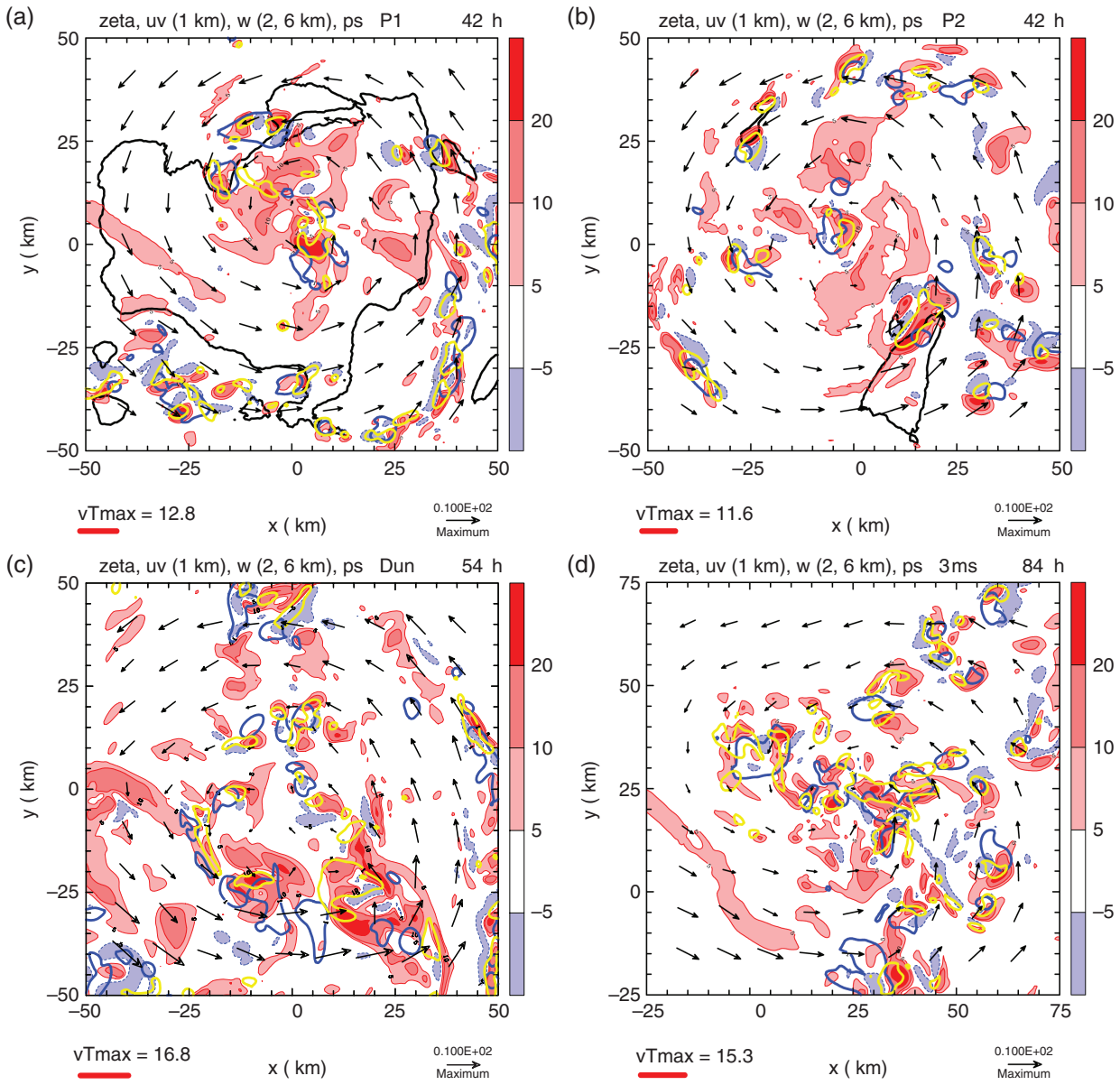

Figure 10. Horizontal cross-sections of relative vertical vorticity ($\times 10^{-4}$ s^{-1}, colour shading), and wind vectors at a height of 1 km for the different sensitivity experiments (a) Expt 2 at 42 h, (b) Expt 3 at 42 h, (c) Expt 4 at 54 h and (d) Expt 5 at 84 h. Also shown are the 1 m s^{-1} contour of vertical velocity at heights of 2 km (blue) and 6 km (yellow), and black contours of surface pressure (at 2 mb intervals). These times are a few hours before the rapid intensification phase begins. The wind vectors relate to the maximum reference vector at the bottom right, while on the bottom left the maximum total wind speed in the domain is given in m s^{-1}.

at selected times just before the intensification begin time for Expts 2–5. Figures 10(a) and (b) should be compared to the control simulation (Figure 3(a)). The stochastic nature of deep convection is evident when comparing these fields at 42 h in Expts 1–3. Despite this stochastic element, the intensification begin time in Expts 1–3 is essentially the same, an indication of the robustness of the results presented herein. However, this lack of sensitivity might be due to the addition of moisture perturbations on the fine grid scale being used. Our computational resources prevent us investigating this possibility at the present time.

The structure of the vorticity fields in Expts 4 and 5 (Figures 10(c) and (d)) reflect also the stochastic nature of deep convection, although the intensification begin time occurs much later in these two experiments. The explanation for the delayed intensification begin time in Expt 4 is presumably because, with the Dunion sounding, the collective effects of deep convection lead to a weaker overturning circulation in the early stages. Despite the fact that the Dunion sounding has larger CAPE than the *Karl* pouch sounding (2104 J kg^{-1} compared to 2028 J kg^{-1}), it has a moderately drier mid-level environment and a lower TPW (51.5 kg m^{-2} compared to 61 kg m^{-2}).

The delayed intensification begin time in Expt 5 is presumably associated with the slower rate of moistening with lower surface wind speeds and the weaker field of initial vorticity available to be concentrated.

6. Discussion and summary of the genesis process

We summarize now some important features of the genesis process seen in the foregoing simulations and compare these with results of previous studies.

First, using the observed *Karl* pouch sounding with warm rain physics only, spin-up to a mature tropical cyclone occurs within a few days, starting with only a weak initial vortex (V_{max} = 5 m s^{-1}) at a radius of 100 km. In the control simulation, during the first 45 h, the middle and upper troposphere progressively warm and humidify (Figures 8(a)–(d)) following the onset of deep convection at about 12 h (Figures 2(e) and 8(e)). This warming and moistening has been found in many previous studies (section 4.3). Deep convection forms within the pouch provided by the initial circulation and becomes progressively focussed near the centre of circulation (the so-called 'sweet spot' as conceived by Dunkerton *et al.*, 2009).

From an azimuthally averaged perspective, the inflow produced by the collective effects of this convection in the lower troposphere draws the *M*-surfaces inwards to spin up the tangential wind,

at least above some shallow boundary layer. The progressive spin-up of the tangential wind is accompanied by a progressive strengthening of boundary-layer inflow, which, in turn, is responsible for focussing the deep convection near the circulation centre (a process termed 'boundary-layer control' by Kilroy *et al.*, 2016).

Because the atmosphere is statically stable to dry ascent, the increasing mass converging in the boundary layer will flow outwards in the lower troposphere unless it can ascend in cloud (e.g. in deep convective cores) where adiabatic cooling is more than offset by latent heat release. That is, the deep convection must be sufficiently buoyant to enable it to ventilate the mass converging in the boundary layer (Kilroy *et al.*, 2016). These processes are just those found responsible for vortex intensification starting with an initial vortex of near tropical storm strength (Nguyen *et al.*, 2008; Montgomery *et al.*, 2009; Smith *et al.*, 2009). The foregoing behaviour is similar in all the other simulations here, but the time at which rapid intensification begins is different.

From a three-dimensional perspective, the genesis process as simulated here is similar also to that when starting with a much stronger initial vortex ($V_{\max} = 15\,\mathrm{m\,s^{-1}}$). In a horizontal plane, the pattern of deep convection is far from axisymmetric during the genesis period, as is the pattern of convectively amplified relative vorticity. A striking finding as mentioned in section 4.2 is that the organization of the relative vorticity into a monopole structure occurs at relatively low wind speeds and before the pressure has fallen substantially.

Barotropic processes play a role in the formation of a monopole of cyclonic vorticity within a few hours near the intensification begin time, but these are greatly reinforced by the convectively induced convergence in the lower troposphere. In turn, the boundary layer exerts a progressive control on the location of deep convection, focussing it near the centre of the emergent low-level vortex monopole circulation.

The relatively rapid formation of this monopole from individual patches of convectively amplified vorticity might be regarded broadly as a tipping point in the intensification process, but there is no single event marking this point. Rather, there appears to be a continuous, but accelerating mutual organization of the vorticity field and the deep convection that produces an inward flux of absolute vorticity in the lower troposphere, the deep convection being supported by a progressive boundary-layer control process.

We noted above that the distribution of convectively amplified vorticity has a stochastic element on account of the stochastic nature of deep convection. This feature must generally add a stochastic element to the vorticity organization process and also the timing of the tipping point, as indicated by the perturbed moisture experiments presented in section 5.

The foregoing summary of the events around the intensification begin time is somewhat different from that offered by Nolan (2007, p. 264). Nolan found that at this time, a 'smaller-scale, surface vortex was created by a single, long-lived updraught that erupts very near the centre of the larger mid-level vortex.' Nolan concluded that 'The trigger for tropical cyclogenesis is the formation of this long-lasting updraught, which organises the low-level vorticity into a single coherent vortex through what might be considered either a repeated or continuous diabatic vortex merger process ...'. As discussed above, we do not find evidence of a single, long-lived updraught around the genesis time. Rather, at the higher spatial resolution employed herein (horizontal grid spacing 500 m compared with 2 km used by Nolan) and without a representation of ice microphysics, we find multiple transient updraughts. Furthermore, as noted above, we are unable to identify any 'trigger' in the thermodynamic or dynamical fields that marks the intensification begin time.

All in all, the rotating-convection paradigm appears adequate to explain basic genesis processes within the pouch, providing strong support for the hypothesis of Montgomery and Smith (2011) that the processes of genesis are not fundamentally different from those of vortex intensification. Moreover, the prior existence of a mid-level vortex is not essential for genesis in calculations where ice microphysical processes are absent (cf. Bister and Emanuel, 1998; Nolan, 2007; Raymond *et al.*, 2011, 2014). Even so, we do not dispute the importance of ice microphysical processes in the generation of a mid-level vortex, which may play a role (albeit not critical) in tropical cyclogenesis in the real atmosphere. This aspect will be examined in a separate study.

7. Conclusions

We have investigated the process of tropical cyclogenesis in a series of idealized, high-resolution, numerical simulations on an f-plane starting with a weak initial vortex (maximum wind speed $5\,\mathrm{m\,s^{-1}}$, or even only $3\,\mathrm{m\,s^{-1}}$, at a radius of 100 km) representing a pouch-like environment without an ambient flow. For simplicity, only warm rain processes associated with deep convection were considered. With this idealization, a mid-level vortex does not develop, suggesting that the prior existence of a mid-level vortex is not essential for genesis. The results support the hypothesis that the process of tropical cyclogenesis within a favourable pouch-like environment with no ambient flow is not fundamentally different from that in the rotating convection paradigm for tropical cyclone intensification. The additional effects of including of ice-microphysical processes will be examined in a forthcoming study.

Acknowledgements

We thank two anonymous reviewers for their perceptive comments on the original manuscript. GK and RKS acknowledge financial support for tropical cyclone research from the German Research Council (Deutsche Forschungsgemeinschaft) under grant numbers SM30/23-3 and SM30/23-4 and the Office of Naval Research Global under grant number N62909-15-1-N021. MTM acknowledges the support of NSF grant AGS-1313948, NOAA HFIP grant N0017315WR00048, NASA grant NNG11PK021 and the US Naval Postgraduate School.

References

Bister M, Emanuel KA. 1998. Dissipative heating and hurricane intensity. *Meteorol. Atmos. Phys.* **65**: 233–240.

Braun SA, Montgomery MT, Mallen KJ, Reasor PD. 2010. Simulation and interpretation of the genesis of Tropical Storm Gert (2005) as part of the NASA Tropical Cloud Systems and Processes Experiment. *J. Atmos. Sci.* **67**: 999–1025.

Bryan GH 2016. 'The governing equations for CM1', Technical Note. UCAR: Boulder, CO. http://www2.mmm.ucar.edu/people/bryan/cm1/cm1_equations.pdf (accessed 23 October 2016).

Bryan GH, Fritsch JM. 2002. A benchmark simulation for moist nonhydrostatic numerical models. *Mon. Weather Rev.* **130**: 2917–2928.

Bryan GH, Rotunno R. 2009. The maximum intensity of tropical cyclones in axisymmetric numerical model simulations. *Mon. Weather Rev.* **137**: 1770–1789.

Davis CA. 2015. The formation of moist vortices and tropical cyclones in idealized simulations. *J. Atmos. Sci.* **72**: 3499–3516.

Davis CA, Ahijevych D. 2012. Mesoscale structural evolution of three tropical weather systems observed during PREDICT. *J. Atmos. Sci.* **69**: 1284–1305.

Dritschel DG, Waugh DW. 1992. Quantification of the inelastic interaction of unequal vortices in two-dimensional vortex dynamics. *Phys. Fluids A* **4**: 1737–1744.

Dunion JP. 2011. Rewriting the climatology of the tropical North Atlantic and Carribean Sea atmosphere. *J. Climate* **24**: 893–908.

Dunkerton TJ, Montgomery MT, Wang Z. 2009. Tropical cyclogenesis in a tropical wave critical layer: Easterly waves. *Atmos. Chem. Phys.* **9**: 5587–5646.

Elsberry RL, Harr P. 2008. Tropical cyclone structure (TCS08) field experiment scientific basis, observational platforms, and strategy. *Asia-Pac. J. Atmos. Sci.* **44**: 1–23.

Emanuel KA. 1989. The finite amplitude nature of tropical cyclogenesis. *J. Atmos. Sci.* **46**: 3431–3456.

Emanuel KA, DesAutels C, Holloway C, Korty R. 2004. Environmental control of tropical cyclone intensity. *J. Atmos. Sci.* **61**: 843–858.

Fang J, Zhang F. 2010. Initial development and genesis of Hurricane Dolly (2008). *J. Atmos. Sci.* **67**: 655–672.

Frank WM. 1987. Tropical cyclone formation. In *A Global View of Tropical Cyclones*, Elsberry RL. (ed.): 53–90. Office of Naval Research: Arlington, VA.

Fritz CL, Wang Z. 2013. A numerical study about the impacts of dry air on tropical cyclone formation. *J. Atmos. Sci.* **70**: 91–111.

Gjorgjievska S, Raymond DJ. 2014. Interaction between dynamics and thermodynamics during tropical cyclogenesis. *Atmos. Chem. Phys.* **14**: 3065–3082.

Hakim GJ. 2011. The mean state of axisymmetric hurricanes in statistical equilibrium. *J. Atmos. Sci.* **68**: 1364–1376.

Hendricks EA, Montgomery MT, Davis CA. 2004. On the role of 'vortical' hot towers in formation of tropical cyclone *Diana* (1984). *J. Atmos. Sci.* **61**: 1209–1232.

Karyampudi VM, Pierce HF. 2002. Synoptic-scale influence of the Saharan air layer on tropical cyclogenesis over the eastern Atlantic. *Mon. Weather Rev.* **130**: 3100–3128.

Kilroy G, Smith RK. 2013. A numerical study of rotating convection during tropical cyclogenesis. *Q. J. R. Meteorol. Soc.* **139**: 1255–1269.

Kilroy G, Smith RK. 2016. A numerical study of deep convection in tropical cyclones. *Q. J. R. Meteorol. Soc.* **142**: 3138–3151, doi: 10.1002/qj.2895.

Kilroy G, Smith RK, Montgomery MT. 2016. Why do model tropical cyclones grow progressively in size and decay in intensity after reaching maturity? *J. Atmos. Sci.* **73**: 487–503.

Komaromi WA. 2013. An investigation of composite dropsonde profiles for developing and nondeveloping tropical waves during the 2010 PREDICT field campaign. *J. Atmos. Sci.* **70**: 542–558.

Lussier LL, Montgomery MT, Bell MM. 2014. The genesis of typhoon *Nuri* as observed during the Tropical Cyclone Structure 2008 (TCS-08) field experiment –Part 3: Kinematical and dynamical aspects of the genesis. *Atmos. Chem. Phys.* **14**: 8795–8812.

McBride JL. 1995. Tropical cyclone formation. In *Global Perspectives on Tropical Cyclones*, WMO/TD-No 693, Elsberry RL. (ed.): 21–62. World Meteorological Organization: Geneva, Switzerland.

Melander MV, McWilliams JC, Zabusky NJ. 1987. Axisymmetrization and vorticity-gradient intensification of an isolated two-dimensional vortex through filamentation. *J. Fluid Mech.* **178**: 137–159.

Melhauser C, Zhang F. 2014. Diurnal radiation cycle impact on the pregenesis environment of hurricane *Karl* (2010). *J. Atmos. Sci.* **71**: 1241–1259.

Montgomery MT, Smith RK. 2011. 'Tropical-cyclone formation: theory and idealized modelling'. In *Proceedings of Seventh WMO International Workshop on Tropical Cyclones (IWTC-VII) La Réunion, November 2010*, (WWRP 2011-1). World Meteorological Organization: Geneva, Switzerland.

Montgomery MT, Smith RK. 2012. The genesis of typhoon *Nuri* as observed during the Tropical Cyclone Structure 2008 (TCS08) field experiment. Part 2: Observations of the convective environment. *Atmos. Chem. Phys.* **120**: 4001–4009.

Montgomery MT, Smith RK. 2017. Recent developments in the fluid dynamics of tropical cyclones. *Annu. Rev. Fluid Mech.* **49**: 541–574.

Montgomery MT, Nicholl ME, Cram TA, Saunders A. 2006. A 'vortical' hot tower route to tropical cyclogenesis. *J. Atmos. Sci.* **63**: 355–386.

Montgomery MT, Nguyen SV, Smith RK, Persing J. 2009. Is WISHE essential for tropical cyclone intensification? *Q. J. R. Meteorol. Soc.* **135**: 1697–1714.

Montgomery MT, Lussier LL, Moore RW, Wang ZW. 2010. The genesis of typhoon *Nuri* as observed during the Tropical Cyclone Structure 2008 (TCS-08) field experiment. Part 1: The role of the easterly wave critical layer. *Atmos. Chem. Phys.* **10**: 9879–9900.

Montgomery MT, Davis C, Dunkerton T, Wang Z, Velden C, Torn R, Majumdar SJ, Zhang F, Smith RK, Bosart L, Bell MM, Haase JS, Heymsfield A, Jensen J, Campos T, Boothe MA. 2012. The Pre-depression Investigation of Cloud systems in the Tropics (PREDICT) experiment: Scientific basis, new analysis tools and some first results. *Bull. Am. Meteorol. Soc.* **93**: 153–172.

Montgomery MT, Persing J, Smith RK. 2015. Putting to rest WISHE-ful misconceptions. *J. Adv. Model. Earth Syst.* **7**: 92–109.

Nicholls M, Montgomery MT. 2013. An examination of two pathways to tropical cyclogenesis occurring in idealized simulations with a cloud-resolving numerical model. *Atmos. Chem. Phys.* **13**: 5999–6022.

Nguyen SV, Smith RK, Montgomery MT. 2008. Tropical-cyclone intensification and predictability in three dimensions. *Q. J. R. Meteorol. Soc.* **134**: 563–582.

Nolan DS. 2007. What is the trigger for tropical cyclogenesis? *Aust. Meteorol. Mag.* **56**: 241–266.

Ooyama KV. 1982. Conceptual evolution of the theory and modeling of the tropical cyclone. *J. Meteorol. Soc. Jpn.* **60**: 369–380.

Park MS, Penny AB, Elsberry RL, Billings BJ, Doyle JD. 2013. Latent heating and cooling rates in developing and nondeveloping tropical disturbances during TCS-08: radar-equivalent retrievals from mesoscale numerical models and ELDORA. *J. Atmos. Sci.* **70**: 37–55.

Persing J, Montgomery MT, McWilliams J, Smith RK. 2013. Asymmetric and axisymmetric dynamics of tropical cyclones. *Atmos. Chem. Phys.* **13**: 12249–12341.

Raymond DJ, López Carillo C. 2011. The vorticity budget of developing typhoon *Nuri* (2008). *Atmos. Chem. Phys.* **11**: 147–163.

Raymond DJ, Sessions SL, López Carrillo C. 2011. Thermodynamics of tropical cyclogenesis in the northwest Pacific. *J. Geophys. Res.* **116**: D18101, doi: 10.1029/2011JD015624.

Raymond DJ, Gjorgjievska S, Sessions S, Fuchs Z. 2014. Tropical cyclogenesis and mid-level vorticity. *Aust. Meteorol. Oceanogr. J.* **64**: 11–25.

Rotunno R, Emanuel KA. 1987. An air–sea interaction theory for tropical cyclones. Part II: Evolutionary study using a nonhydrostatic axisymmetric numerical model. *J. Atmos. Sci.* **44**: 542–561.

Saunders A, Montgomery MT. 2004. A closer look at vortical hot towers within a tropical cyclogenesis environment, Atmospheric Science Bluebook No. 752. Colorado State University: Fort Collins, CO.

Shin S, Smith RK. 2008. Tropical-cyclone intensification and predictability in a minimal three-dimensional model. *Q. J. R. Meteorol. Soc.* **134**: 1661–1671.

Smith RK. 2006. Accurate determination of a balanced axisymmetric vortex. *Tellus* **58A**: 98–103.

Smith RK, Montgomery MT. 2010. Hurricane boundary-layer theory. *Q. J. R. Meteorol. Soc.* **136**: 1665–1670.

Smith RK, Montgomery MT. 2012. Observations of the convective environment in developing and non-developing tropical disturbances. *Q. J. R. Meteorol. Soc.* **138**: 1721–1739.

Smith RK, Montgomery MT, Nguyen SV. 2009. Tropical-cyclone spin up revisited. *Q. J. R. Meteorol. Soc.* **135**: 1321–1335.

Smith RK, Kilroy G, Montgomery MT. 2015. Why do model tropical cyclones intensify more rapidly at low latitudes? *J. Atmos. Sci.* **72**: 1783–1804.

Tory K, Frank WM. 2010. Tropical cyclone formation. In Chapter 2 of *Global Perspectives on Tropical Cyclones: From Science to Mitigation*, Kepert JD, Chan JCL. (eds), Series on Asia-Pacific Weather and Climate **4** World Scientific: Singapore.

Wang Z. 2012. Thermodynamic aspects of tropical cyclone formation. *J. Atmos. Sci.* **69**: 2433–2451.

Wang Z. 2014. Role of cumulus congestus in tropical cyclone formation in a high-resolution numerical model simulation. *J. Atmos. Sci.* **71**: 1681–1700.

Wang Z, Montgomery MT, Dunkerton TJ. 2010. Genesis of pre-hurricane *Felix* (2007). Part I: The role of the easterly wave critical layer. *J. Atmos. Sci.* **67**: 1711–1729.

Wang Z, Montgomery MT, Fritz C. 2012. A first look at the structure of the wave pouch during the 2009 PREDICT-GRIP dry runs over the Atlantic. *Mon. Weather Rev.* **140**: 1144–1163.

Wissmeier U, Smith RK. 2011. Tropical-cyclone convection: The effects of ambient vertical vorticity. *Q. J. R. Meteorol. Soc.* **137**: 845–857.

